

# Numerical studies of dynamic behavior of liquid film on single-layer wire mesh with different wettabilities

Hai-Long Liao<sup>1,2</sup>, Lan Jiang<sup>1,2</sup>, Hai-Xin Yu<sup>1,2</sup>, Zhi-Hao Liu<sup>1,2</sup>, Ji-Wen Fu (✉)<sup>1,2</sup>,  
Guang-Wen Chu<sup>1,2</sup>, Yong Luo (✉)<sup>1,2</sup>

<sup>1</sup> State Key Laboratory of Organic-Inorganic Composites, Beijing University of Chemical Technology, Beijing 100029, China

<sup>2</sup> Research Center of the Ministry of Education for High Gravity Engineering and Technology, Beijing University of Chemical Technology, Beijing 100029, China

© Higher Education Press 2022

**Abstract** Droplet impacting on the stainless steel wire mesh is very common in chemical devices, like a rotating packed bed. Surface wettability of wire mesh significantly affects the liquid flow pattern and liquid dispersion performance. However, the effect of surface wettability on the impaction phenomena at microscale such as liquid film is still unknown. In this work, the dynamic behavior of liquid film on the surface of wire mesh was analyzed by computational fluid dynamics simulation. The dynamic behavior of liquid film on the surface of wire mesh can be divided into the following three steps: (1) spreading step; (2) shrinkage process; (3) stabilizing or disappearing step. Effects of surface wettability, as well as operating conditions, on wetting area and liquid film thickness were studied. Compared to the hydrophilic wire mesh, the final wetting area of hydrophobic wire mesh is zero in most cases. The average liquid film thickness on the surface of hydrophilic wire mesh is 30.02–77.29  $\mu\text{m}$ , and that of hydrophobic wire mesh is 41.76–237.37  $\mu\text{m}$ . This work provided a basic understanding of liquid film flow at microscale on the surface with various surface wettabilities, which can be guiding the packing optimization and design.

**Keywords** stainless steel wire mesh, computational fluid dynamics, surface wettability, liquid film, impacting

## 1 Introduction

In chemical reactors, liquid flow and dispersion significantly affect the gas–liquid or liquid–liquid mass transfer efficiency [1–6]. In packed towers [7,8] or

rotating packed beds [9–11], stainless steel wire mesh (SSM), woven by fibers, is commonly used as a packing. Liquid is dispersed into small droplets or ligaments by impacting on SSM to increase the gas–liquid or liquid–liquid contact area [12–14]. Investigating the process of droplet impacting on SSM is beneficial to reveal the mass transfer performance of chemical reactor.

Surface wettability influences the phenomena of droplet impacting on the single-fiber, single-layer or multilayer SSM. Liu et al. [15] investigated the dispersion phenomena of droplet impacting on single-fiber with different wettabilities. When the contact angle increased from 45° to 155°, the gas–liquid interface area increased by 83% and the energy utilization efficiency increased from 1.97% to 48.29%. Ryu et al. [16] studied the penetration behavior of droplet impacting on single-layer SSM. The liquid was easier to penetrate the superhydrophobic SSM during the impaction, in comparison with hydrophobic SSM. Su et al. [17] employed multilayer SSM to disperse the liquid droplet. The cone angle of dispersion enlarged by 44% and average diameter of daughter droplets decreased by 12% on average when the contact angle of the SSM increased from  $\alpha$ -70° to  $\alpha$ -155°. The above studies focused on the effect of surface wettability on impaction phenomena at macroscale, usually by the means of a high-speed camera to record the impaction behaviors. The liquid film generated on the surface of SSM affected the liquid impaction and dispersion performance. And the behavior was more complicated for a droplet impacting on the surface that's coated by the liquid film, compared to the dry surface [18,19]. It is necessary to illustrate the characteristics of liquid film on the surface.

The high-speed photography technology is usually employed to capture the macroscopic fluid flow, while computational fluid dynamics (CFD) can be used to obtain the microscale thickness of the dynamic liquid film in most cases at a low cost [20–22]. Sun et al. [23] used

Received April 1, 2022; accepted May 29, 2022

E-mails: fujw@mail.buct.edu.cn (Fu J.-W.), luoyong@mail.buct.edu.cn (Luo Y.)

two-dimension configuration to study the flow characteristics of liquid film on horizontally circular tubes. The results showed that the liquid film thickness depended on flow rate and angular distribution. Xu et al. [9] used CFD simulation to study the dynamic behavior of liquid film on the surface of rotating wire meshes, and the average liquid film thickness ( $\delta_{avg}$ ) was 21–32  $\mu\text{m}$ . Xue et al. [24] established a small-scale three-dimension CFD method to simulate the liquid film on the surface of wire mesh. The liquid film thickness of the lower side of the wire mesh was larger than that of the upper side, and the ratio of liquid film thickness between the lower side and upper side was about 5:3. However, the mechanism of the influence of wire mesh's surface wettability on the dynamic behavior of liquid film at microscale was still unclear.

In this work, the effect of surface wettability on the liquid film during droplet impacting on the SSM was investigated through CFD simulation that is easy to capture the liquid film information. The dynamic behavior of liquid film was firstly studied. The velocity vector analysis was then used to reveal the mechanism of the influence of surface wettability on the liquid film. The effect of surface wettability, represented by water contact angle ( $\alpha$ ), on the wetting area and liquid film thickness were systematically investigated. Besides, the effects of initial droplet velocity ( $u_0$ ) and mother droplet diameter ( $D_0$ ) on the wetting area and liquid film thickness were also discussed.

## 2 CFD simulation

### 2.1 Geometry and grid

Figure 1 shows the schematic diagram of compute domain and grid. Figure 1(a) displays the computational domains of liquid impactation on SSM. It has three zones, named as upper zone, impactation zone, and lower zone. Figure 1(b) shows the structure of the SSM. The fiber diameter ( $d_0$ ) and opening size ( $l_0$ ) of the SSM are 0.24 and 0.98 mm respectively. Due to the irregularity of the SSM, tetrahedral meshes were generated in the impactation zone. Local grid refinement was performed on the fiber, and five boundary layers were set on the fiber surface. The thickness of the first layer was 0.01 mm and the growth rate was 1.2. The upper zone and lower zone had the hexahedral structured grid. Grid independence testing has been conducted in the previous study and the same grid with 17584899 was selected for the simulation [25].

### 2.2 Mathematical modeling

The liquid phase is set to water and the gas phase to air, both of which are considered as incompressible and isothermal fluid. In order to capture the gas–liquid interface, the volume of fluid (VOF) model was employed [26–28]. The governing equations of the VOF model are

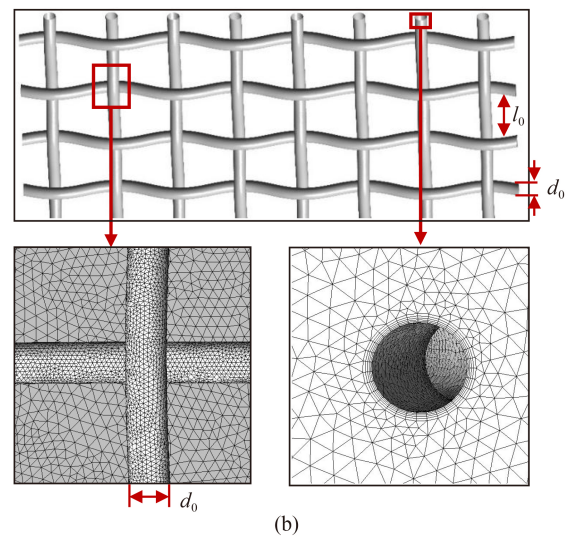
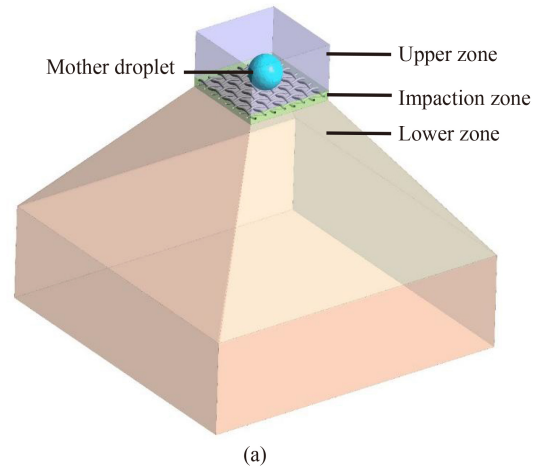


**Fig. 1** Images of (a) 3D computational domains and (b) local meshes of single-layer woven SSM.

listed as follows. The continuous equation is given by:

$$\frac{\partial(\alpha_q \rho_q)}{\partial t} + \nabla \cdot (\alpha_q \rho_q \mathbf{u}_q) = 0. \quad (1)$$

The momentum conservation equation is given by:

$$\frac{\partial(\rho \mathbf{u})}{\partial t} + \nabla \cdot (\rho \mathbf{u} \mathbf{u}) = -\nabla p + \nabla [\mu(\nabla \mathbf{u} + \nabla \mathbf{u}^T)] + \rho \mathbf{g} + \mathbf{F}_v, \quad (2)$$

where  $q$  represents the phase,  $q = \text{L or G}$ . L represents the liquid phase and G represents the gas phase.  $\alpha_q$  represents the volume fraction of the different phases. Liquid viscosity ( $\mu$ ) and density ( $\rho$ ) are defined as:

$$\rho = \sum \alpha_q \rho_q, \mu = \sum \alpha_q \mu_q. \quad (3)$$

The surface tension is introduced as the source term of the momentum conservation equation and defined by the continuous surface force model [29]:

$$\mathbf{F}_v = \sigma \frac{\rho \kappa \nabla \alpha_q}{0.5(\rho_L + \rho_G)}, \quad (4)$$

where  $\kappa = \nabla \cdot \hat{\mathbf{n}}$ ,  $\hat{\mathbf{n}} = \mathbf{n} / |\mathbf{n}|$  and  $\mathbf{n} = \nabla \alpha_q$ . In this work,  $\sigma$  is the coefficient of surface tension of water in air and the value of

$72.67 \text{ mN}\cdot\text{m}^{-1}$  is adopted [30]. Surface wettability is reflected by the contact angle between water and SSM surface.

### 2.3 Boundary conditions and calculation procedure

The operating conditions of simulation calculation are listed in Table 1. All surfaces of the fiber are defined as no slip boundary conditions. The adjacent zone was set as interface. The other boundaries are set as pressure-outlet. Realizable  $k\text{-}\varepsilon$  model was selected [31]. The time step of the calculation was set as  $1 \times 10^{-6}$  s to ensure that the global Courant number was less than 2. The convergence criterions were set as  $1 \times 10^{-3}$ . All case calculations were performed at a DM3 workstation (DYFLUID Ltd.) with two AMD EPYC 7502 32-Core Processor 2.5 GHz and random access memory 128 GB.

**Table 1** Operating conditions

Item	Value
$\alpha/(\text{°})$	70, 110, 130, 155
$u_0/(\text{m}\cdot\text{s}^{-1})$	1.31, 2.50, 3.15, 4.17, 5.10
$D_0/\text{mm}$	2.51, 2.98, 3.50, 3.98, 4.55

### 2.4 Validation for CFD simulation

Based on our previous work, CFD simulation has been verified in detail [25]. On one hand, the simulation results were in good agreement with the experimental results, which qualitatively demonstrated the reasonability of the simulation method; on the other hand, the liquid cone angle of dispersion between simulated and experimental results under identical conditions were quantitatively compared, which proved the accuracy of the simulation method used in this work.

## 3 Results and discussion

### 3.1 Dynamic behavior of liquid film on SSM surface

Figure 2 shows the dynamic behavior of liquid film on hydrophilic and hydrophobic SSM. Figure 2(a) illustrates the dynamic process of droplet impacting on the hydrophilic SSM from top view. Prior to the impaction, the droplet displayed as a regular sphericity due to the

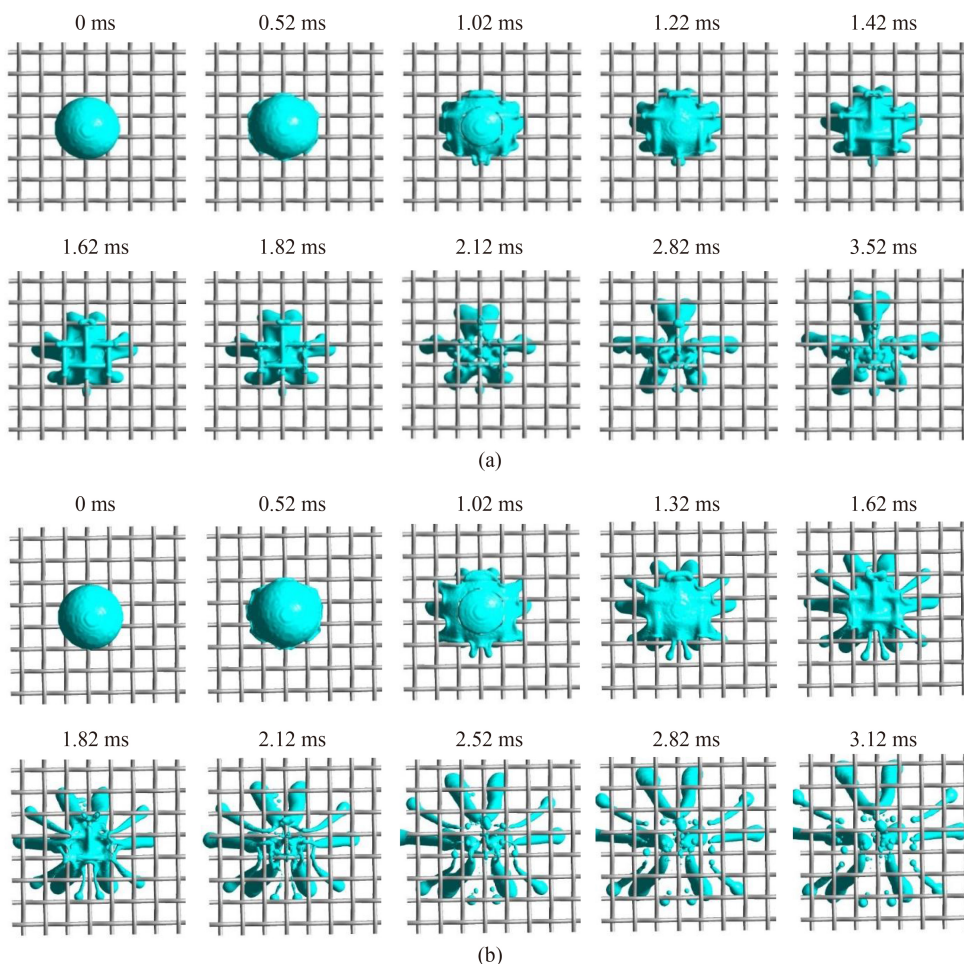


**Fig. 2** (a) Dynamic behavior of liquid film on hydrophilic SSM at  $u_0 = 3.15 \text{ m}\cdot\text{s}^{-1}$ ,  $D_0 = 3.50 \text{ mm}$ ; (b) dynamic behavior of liquid film on hydrophobic SSM at  $u_0 = 3.15 \text{ m}\cdot\text{s}^{-1}$ ,  $D_0 = 3.50 \text{ mm}$ .

surface tension. The droplet was cut by the fiber when the droplet contacted with the SSM. The partial liquid penetrated the holes of the SSM to form liquid jets, which can be further broken into daughter droplets. While the residual liquid was existing in the form of liquid film on the surface of the SSM. The dynamic behavior of liquid film on the surface of SSM can be divided into the following three steps: (1) Liquid film spreading step: the liquid on the upper surface of SSM was still presented as a regular hemispherical shape when the time is 0.52 ms. As the time went by, the liquid that did not penetrate the SSM quickly spread on the SSM surface. During the liquid film spreading process, the wetting area of the liquid film on the SSM surface increased rapidly, accompanied with the decrease of the liquid film thickness; (2) liquid film shrinkage process: the liquid film shrunk along the fiber surface due to the action of surface tension. At this stage, the wetting area of the liquid film gradually decreased with the increment of liquid film thickness; (3) liquid film was stabilizing or disappearing from the surface.

Figure 2(b) displays the dynamic evolution of droplet impacting on the hydrophobic SSM. There was no

obvious difference between the hydrophilic and hydrophobic SSM at spreading step. During (2) and (3) processes, some liquid film was residual on the hydrophilic SSM surface with a shape of hemispherical or spherical. However, the liquid film on the hydrophobic SSM was quickly departed from the surface in 2.52 ms.

### 3.2 Velocity vector analysis of liquid film on wire mesh

Figure 3 shows the velocity vector of liquid film on the surface of hydrophilic and hydrophobic SSM at different times. During spreading process, there was a subtle difference between the spreading direction of liquid film on hydrophilic and hydrophobic SSM surfaces, but the spreading speed of liquid film had some differences. When the time was 1.02 ms, the liquid film spreading speed on hydrophilic SSM surface was  $1.44 \text{ m}\cdot\text{s}^{-1}$ , while the liquid film on the hydrophobic surface moved with an average speed of  $1.61 \text{ m}\cdot\text{s}^{-1}$ . At the same time, the liquid film on the surface of hydrophobic SSM spread to cover more wire mesh holes, which further influenced the cone angle of dispersion and average diameter of daughter droplets.

The liquid film gradually shrunk on account of the

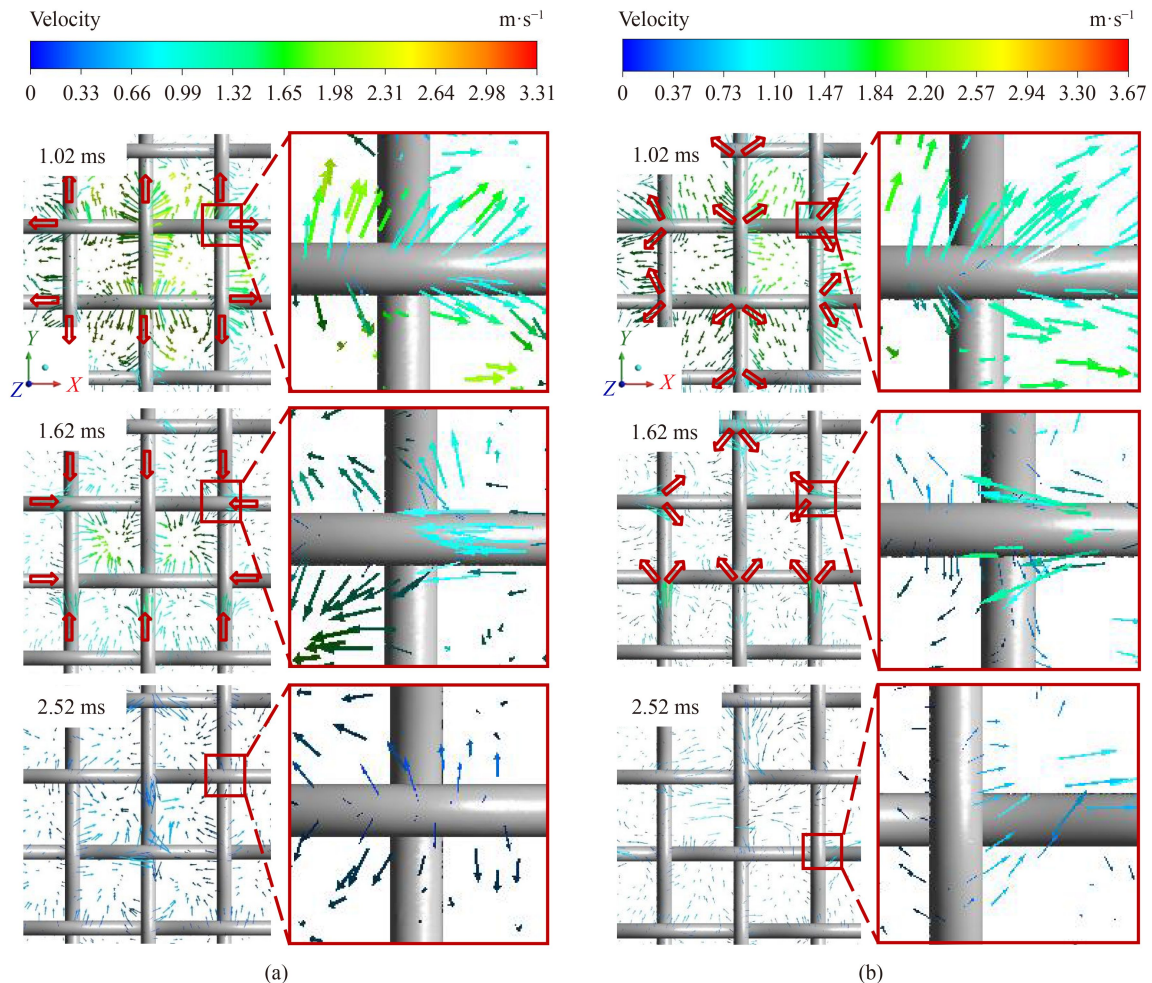


Fig. 3 Velocity vector of liquid film on the SSM surface. (a)  $\alpha=70^\circ$ ; (b)  $\alpha=155^\circ$ .

surface tension. In the stage of liquid film shrinkage, at 1.62 ms as shown in Fig. 3, the shrinkage direction of the liquid film on the hydrophilic SSM was major along with the X and Y axes. Instead, the direction of velocity vector on the hydrophobic surface was multidirectional. And the average shrinkage speed at hydrophilic and hydrophobic SSM were  $1.08$  and  $1.22 \text{ m}\cdot\text{s}^{-1}$ , respectively. The larger shrinkage speed at the hydrophobic surface aroused from the less consumed energy relative to the hydrophilic wire meshes. Accordingly, the maximum wetting area would become smaller on the hydrophobic SSM.

During the liquid film stabilizing or disappearing process, agreeing with the dynamic images, the liquid film speed on the hydrophilic surface was zero at the time of 2.52 ms, indicating that the kinetic energy of liquid film was used up due to the large adhesion force of hydrophilic wire meshes. However, the speed of liquid film on the hydrophobic surface still existed, resulting in the rebounded daughter droplets. It was further indicated that the liquid film on the hydrophobic surface can overcome the adhesion of SSM surface to achieve a better liquid dispersion.

The above qualitative analysis presented the dynamic behaviors of liquid film on SSM surface with different wettabilities by CFD simulation. It was found that the wettabilities have a certain effect on the spreading and shrinkage step, but a remarkable effect on the stabilizing or disappearing process of liquid film. Effects of different operating conditions on liquid film were further quantitatively investigated in the following analysis.

### 3.3 Effect of operating conditions on wetting area and liquid film thickness

The wetting area and liquid film thickness on the SSM surface can provide baseline for the understanding of droplet dispersion and broken mechanism. Compared to high-speed cameras or optical probes with macroscale (millimeter magnitude), the CFD simulation can intuitively observe the dynamic behavior and static

characteristics of liquid film, as well as wetting area and liquid film thickness, on the surface of SSM at microscale (micrometer magnitude).

#### 3.3.1 Wetting area

Figure 4 illustrates the effect of surface wettability on the wetting area at  $u_0 = 3.15 \text{ m}\cdot\text{s}^{-1}$ ,  $D_0 = 3.50 \text{ mm}$ . The required time to reach a stable wetting area was the same although the surface wettabilities were different, while the surface wettability significantly affected the value of wetting area. The hydrophobic surface intensified the shrinkage and disappearance of liquid film, which caused the decrease of residual liquid and low wetting area. Particularly, the liquid on SSM totally disappeared on the surface of  $\alpha\text{-}155^\circ$  when the time was greater than 3 ms. However, on the hydrophilic SSM ( $\alpha\text{-}70^\circ$ ), much liquid remained on the surface.

Figure 5 illustrates the effect of  $u_0$  on the wetting area of SSM. Figures 5(a) and 5(b) display the wetting area of hydrophilic SSM and hydrophobic SSM, respectively. With the increase of  $u_0$ , the time for liquid film disappearance gradually decreased on both hydrophilic

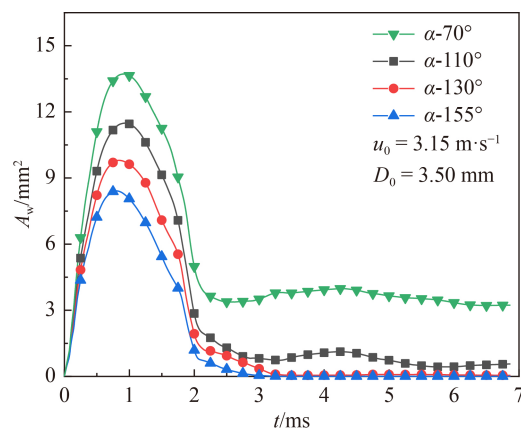


Fig. 4 Effect of surface wettability of SSM on the wetting area at  $u_0 = 3.15 \text{ m}\cdot\text{s}^{-1}$ ,  $D_0 = 3.50 \text{ mm}$ .

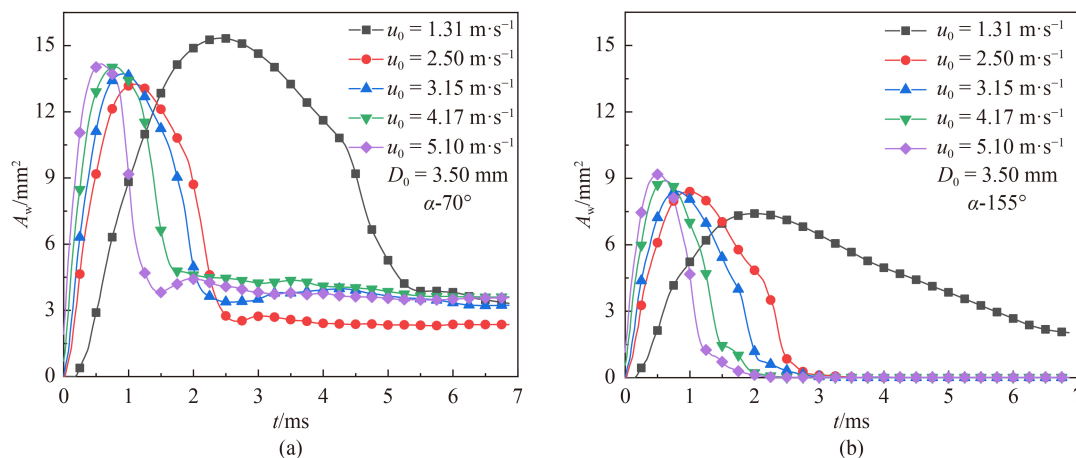


Fig. 5 Effects of (a)  $\alpha\text{-}70^\circ$  and (b)  $\alpha\text{-}155^\circ$  on the wetting area at different initial droplet velocities.

and hydrophobic SSM. The possible reason is that when the speed was higher, the larger kinetic energy was easier to overcome the dissipation energy of the SSM, which would intensify the process of liquid film spreading and shrinking. The difference of wetting areas between hydrophilic and hydrophobic SSM was ascribed to liquid film flow behavior on the surface.

Figure 6 illustrates the effect of  $D_0$  on the wetting area of SSM. Figures 6(a) and 6(b) display the wetting area of hydrophilic SSM and hydrophobic SSM, respectively. The time for reaching a stable wetting area increased with the increment of  $D_0$ . The wetting area on the hydrophilic surface was greater than that of the

hydrophobic surface with the same droplet diameter. The final wetting area was none-zero on the hydrophilic SSM, while it was zero on the hydrophobic SSM. Compared to the surface with no liquid, the energy consumption would be higher during the impaction on the SSM surface coated by liquid film, whereafter affecting the liquid dispersion performance and the diameter of daughter droplets.

### 3.3.2 Liquid film thickness

A calculation method for obtaining the instantaneous liquid film thickness was developed in this work. Figure 7

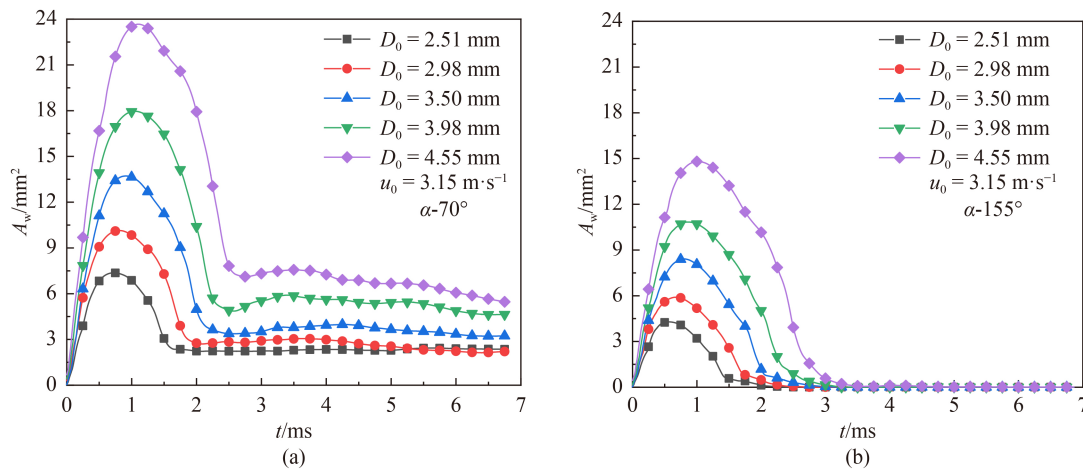


Fig. 6 Effects of (a)  $\alpha=70^\circ$  and (b)  $\alpha=155^\circ$  on the wetting area at different mother droplet diameters.

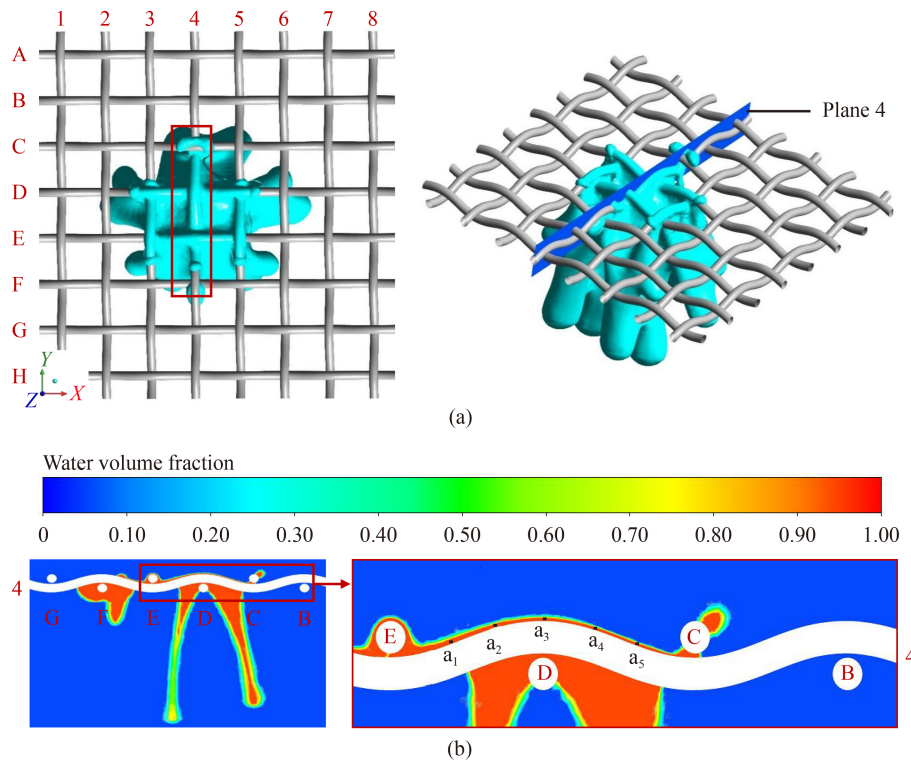
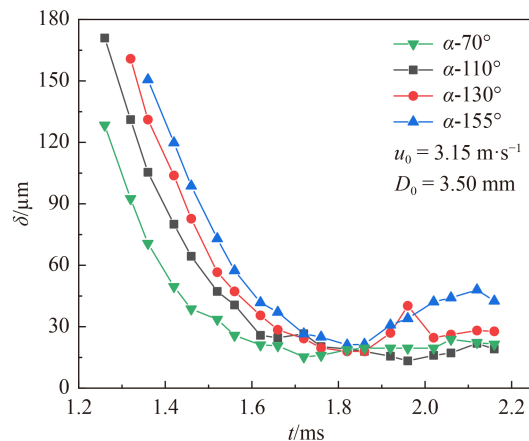


Fig. 7 Schematic diagram of liquid film thickness measurement. (a) Selection of cross-section; (b) an example of a liquid film thickness measurement for plane 4.

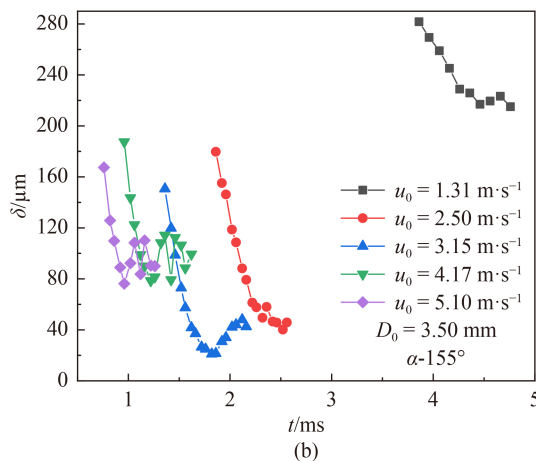
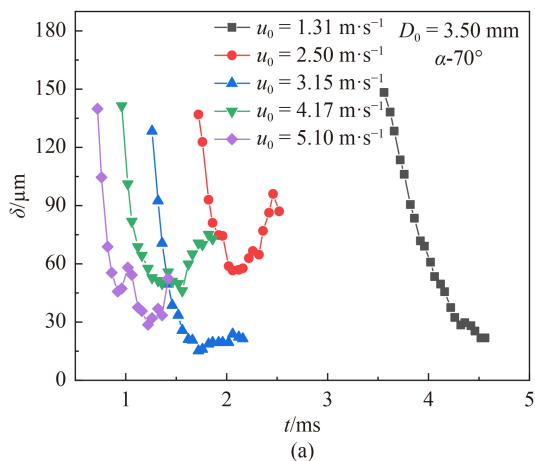
shows the schematic diagram of liquid film thickness measurement. As shown in Fig. 7(a), the liquid covered five fibers, and the liquid film thickness at this moment was an average value of liquid film thicknesses on these five fibers. Figure 7(b) displays that five points were selected between point C and point E to measure liquid film thickness.

Figure 8 shows the effect of surface wettability on the instantaneous liquid film thickness at  $u_0 = 3.15 \text{ m}\cdot\text{s}^{-1}$ ,  $D_0 = 3.50 \text{ mm}$ . When the time was smaller than 1.6 ms, the value of liquid film thickness on the hydrophilic SSM was less than the thickness on the hydrophobic SSM. With the increase of time ( $> 1.6 \text{ ms}$ ), the liquid film thickness showed a slight increment due to the liquid film shrinkage. Figure 9 displays the influence of  $u_0$  on the instantaneous liquid film thickness. The time for reaching the minimum thickness decreased with the increment of  $u_0$  from 2.50 to  $5.1 \text{ m}\cdot\text{s}^{-1}$ . At the low speed of  $u_0 = 1.31 \text{ m}\cdot\text{s}^{-1}$ , the droplet remained on wire mesh for a long time. The initial speed of droplet played a role on the spreading and shrinkage of the liquid film, leading to the change of film thickness. Figure 10 presents that with the

increment of  $D_0$ , the time for achieving the minimum thickness increased. At the same  $D_0$ , the liquid on the hydrophilic SSM reached the minimum liquid film thickness with a shorter time compared with the hydrophobic SSM.



**Fig. 8** Effect of surface wettability of SSM on the liquid film thickness at  $u_0 = 3.15 \text{ m}\cdot\text{s}^{-1}$ ,  $D_0 = 3.50 \text{ mm}$ .



**Fig. 9** Effects of (a)  $\alpha=70^\circ$  and (b)  $\alpha=155^\circ$  on the liquid film thickness at different initial droplet velocities.

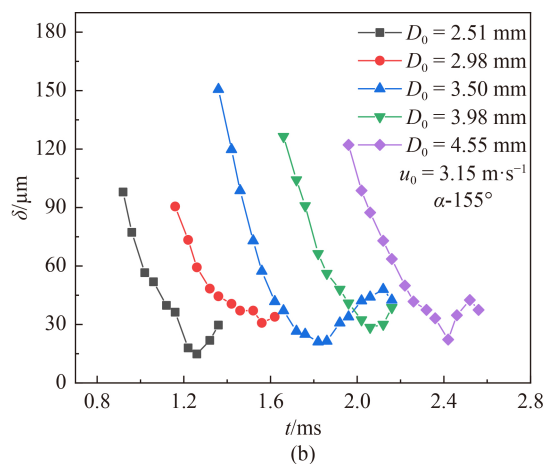
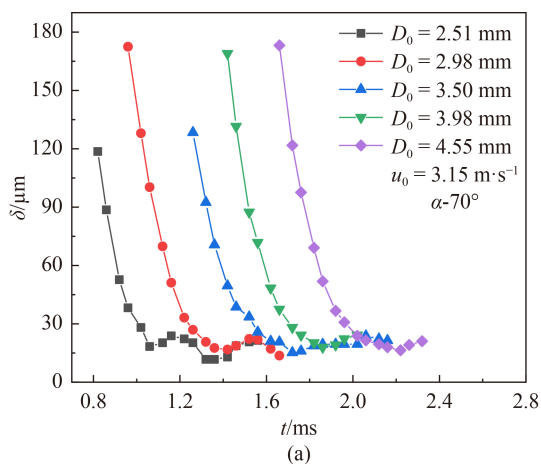


**Fig. 10** Effects of (a)  $\alpha=70^\circ$  and (b)  $\alpha=155^\circ$  on the liquid film thickness at different mother droplet diameters.

The instantaneous liquid film thickness provided much information to understand the impaction process. In order to intuitively illustrate the effect of surface wettability and operation condition on the liquid film thickness, the  $\delta_{avg}$  based on the instantaneous thickness was calculated by:

$$\delta_{avg} = \frac{\int_{t_1}^{t_2} \delta dt}{t_2 - t_1} = \frac{\sum_{t_1}^{t_2} \delta \Delta t}{t_2 - t_1}, \quad (5)$$

where  $t_1$  is the time at the beginning of liquid penetrating the wire mesh,  $t_2$  is the time at the beginning of stabilizing or disappearing on the surface,  $\delta$  is liquid film thickness. Tables 2 and 3 show the calculated results of  $\delta_{avg}$ . As shown in Table 2,  $\delta_{avg}$  did not change significantly with the increase of  $\alpha$ . Table 3 shows the effect of  $u_0$  on the  $\delta_{avg}$ . When  $u_0$  was smaller than  $3.15 \text{ m}\cdot\text{s}^{-1}$ ,  $\delta_{avg}$  decreased with the increase of  $u_0$ . When  $u_0$  was bigger than  $3.15 \text{ m}\cdot\text{s}^{-1}$ ,  $\delta_{avg}$  increased with the increment of  $u_0$ , which can be attributed that the residence time of the liquid film on the surface of the SSM became shorter. Besides,  $\delta_{avg}$  increased with the increment of  $D_0$ .

### 4 Conclusions

The dynamic behavior of liquid film on SSM surface was analyzed by CFD simulation, and the influence of different operating conditions on its wetting area and liquid film thickness was studied. It can be found that the dynamic behavior of liquid film on the surface of SSM can be divided into three processes of spreading process, shrinkage process, and stabilizing or disappearing process. The liquid film was retained on the surface of the

hydrophilic SSM and shrunk to hemispherical or spherical liquid group. The wetting area and liquid film thickness tended to be constant. The  $\delta_{avg}$  of hydrophilic SSM was  $30.02\text{--}77.29 \mu\text{m}$ , and that of hydrophobic SSM was  $41.76\text{--}237.37 \mu\text{m}$ . The numerical simulation results of liquid film not only help to know the impaction behavior, but also help to understand the subsequent dispersion performance.

**Acknowledgments** This work was supported by the National Natural Science Foundation of China (Grant No. 22022802).

### References

- Sun B C, Dong K, Zhao W, Wang J W, Chu G W, Zhang L L, Zou H K, Chen J F. Simultaneous absorption of  $\text{NO}_x$  and  $\text{SO}_2$  into  $\text{Na}_2\text{SO}_3$  solution in a rotating packed bed with preoxidation by ozone. *Industrial & Engineering Chemistry Research*, 2019, 58(19): 8332–8341
- Luo Y, Luo J Z, Chu G W, Zhao Z Q, Arowo M, Chen J F. Investigation of effective interfacial area in a rotating packed bed with structured stainless steel wire mesh packing. *Chemical Engineering Science*, 2017, 170: 347–354
- Wang P H, Zhuang L W, Dai G. Synergistic effect of droplet self-adjustment and rod bank internal on fluid distribution in a WFGD spray column. *Chemical Engineering Science*, 2017, 162: 227–244
- Chen Q Y, Chu G W, Luo Y, Sang L, Zhang L L, Zou H K, Chen J F. Polytetrafluoroethylene wire mesh packing in a rotating packed bed: mass transfer studies. *Industrial & Engineering Chemistry Research*, 2016, 55(44): 11606–11613
- Fourati M, Roig V, Raynal L. Experimental study of liquid spreading in structured packings. *Chemical Engineering Science*, 2012, 80: 1–15
- Guo F, Chong Z, Guo K, Feng Y D, Gardner N C. Hydrodynamics and mass transfer in cross-flow rotating packed bed. *Chemical Engineering Science*, 1997, 52(21–22): 3853–3859
- Schubert M, Hamidipour M, Duchesne C, Larachi F. Hydrodynamics of cocurrent two-phase flows in slanted porous media-modulation of pulse flow via bed obliquity. *AIChE Journal*, 2010, 56(12): 3189–3205
- Spiegel L, Meier W. Distillation columns with structured packings in the next decade. *Chemical Engineering Research & Design*, 2003, 81(1): 39–47
- Xu Y C, Li Y B, Liu Y Z, Luo Y, Chu G W, Zhang L L, Chen J F. Liquid jet impaction on the single-layer stainless steel wire mesh in a rotating packed bed reactor. *AIChE Journal*, 2019, 65(6): e16597
- Chu G W, Gao X, Luo Y, Zou H K, Shao L, Chen J F. Distillation studies in a two-stage counter-current rotating packed bed. *Separation and Purification Technology*, 2013, 102: 62–66
- Luo Y, Chu G W, Zou H K, Zhao Z Q, Dudukovic M P, Chen J F. Gas–liquid effective interfacial area in a rotating packed bed. *Industrial & Engineering Chemistry Research*, 2012, 51(50): 16320–16325

**Table 2**  $\delta_{avg}$  at different surface wettabilities of SSM

$\alpha/(\circ)$	$u_0/(\text{m}\cdot\text{s}^{-1})$	$D_0/\text{mm}$	$\delta_{avg}/\mu\text{m}$
70	3.15	3.50	51.81
110	3.15	3.50	54.16
130	3.15	3.50	52.54
155	3.15	3.50	51.76

**Table 3**  $\delta_{avg}$  at different initial droplet velocities and mother droplet diameters

$\alpha/(\circ)$	$u_0/(\text{m}\cdot\text{s}^{-1})$	$D_0/\text{mm}$	$\delta_{avg}/\mu\text{m}$	$\alpha/(\circ)$	$u_0/(\text{m}\cdot\text{s}^{-1})$	$D_0/\text{mm}$	$\delta_{avg}/\mu\text{m}$
70	1.31	3.50	77.29	155	1.31	3.50	237.37
70	2.50	3.50	65.59	155	2.50	3.50	73.84
70	3.15	3.50	51.81	155	3.15	3.50	51.76
70	4.17	3.50	65.87	155	4.17	3.50	87.27
70	5.10	3.50	67.22	155	5.10	3.50	94.64
70	3.15	2.51	30.02	155	3.15	2.51	41.76
70	3.15	2.98	46.67	155	3.15	2.98	48.46
70	3.15	3.50	51.81	155	3.15	3.50	51.76
70	3.15	3.98	52.73	155	3.15	3.98	58.89
70	3.15	4.55	53.55	155	3.15	4.55	62.30

12. Nygaard H G, Kiil S, Johnsson J E, Jensen J N, Hansen J, Fogh F, Dam-Johansen K. Full-scale measurements of SO<sub>2</sub> gas phase concentrations and slurry compositions in a wet flue gas desulphurisation spray absorber. *Fuel*, 2004, 83(9): 1151–1164
13. Gololo K V, Majozi T. Complex cooling water systems optimization with pressure drop consideration. *Industrial & Engineering Chemistry Research*, 2013, 52(22): 7056–7065
14. Ma J, Irfan H M, Wang Y F, Feng X, Xu D M. Recovering wastewater in a cooling water system with thermal membrane distillation. *Industrial & Engineering Chemistry Research*, 2018, 57(31): 10491–10499
15. Liu Z H, Li Y B, Su M J, Luo Y, Chu G W. Dispersion phenomena of liquid droplet impacting on the single fiber with different wettabilities. *Chemical Engineering Science*, 2022, 248: 117169
16. Ryu S, Sen P, Nam Y, Lee C. Water penetration through a superhydrophobic mesh during a drop impact. *Physical Review Letters*, 2017, 118(1): 014501
17. Su M J, Luo Y, Chu G W, Cai Y, Le Y, Zhang L L, Chen J F. Intensification of droplet dispersion by using multilayer wire mesh and its application in a rotating packed bed. *Industrial & Engineering Chemistry Research*, 2020, 59(8): 3584–3592
18. Manzello S L, Yang J C. An experimental study of a water droplet impinging on a liquid surface. *Experiments in Fluids*, 2002, 32(5): 580–589
19. Xie H, Koshizuka S, Oka Y. Modelling of a single drop impact onto liquid film using particle method. *International Journal for Numerical Methods in Fluids*, 2004, 45(9): 1009–1023
20. Lu X, Du X, Zeng M, Zhang S, Wang Q. Shell-side thermal-hydraulic performances of multilayer spiral-wound heat exchangers under different wall thermal boundary conditions. *Applied Thermal Engineering*, 2014, 70(2): 1216–1227
21. Tahir F, Mabrouk A, Koc M. Review on CFD analysis of horizontal falling film evaporators in multi effect desalination plants. *Desalination and Water Treatment*, 2019, 166: 296–320
22. Wang Q F, Li M X, Xu W J, Yao L, Liu X T, Su D D, Wang P. Review on liquid film flow and heat transfer characteristics outside horizontal tube falling film evaporator: CFD numerical simulation. *International Journal of Heat and Mass Transfer*, 2020, 163: 120440
23. Sun F D, Xu S L, Gao Y C. Numerical simulation of liquid falling film on horizontal circular tubes. *Frontiers of Chemical Science and Engineering*, 2012, 6(3): 322–328
24. Xue J X, Li Q S, Qi J, Wu Q P, Zhao H K, Zhang L Q. Multi-scale study of wet pressure drop model for a novel structured wire gauze packing. *Chemical Engineering Science*, 2021, 230: 116179
25. Liao H L, Ouyang Y, Zhang J P, Zou H K, Chu G W, Luo Y. Numerical studies of liquid droplet impacting on single-layer hydrophilic and hydrophobic wire meshes. *Industrial & Engineering Chemistry Research*, 2022, 61(20): 7154–7162
26. Xie P, Lu X S, Yang X, Ingham D, Ma L, Pourkashanian M. Characteristics of liquid flow in a rotating packed bed for CO<sub>2</sub> capture: a CFD analysis. *Chemical Engineering Science*, 2017, 172(23): 216–229
27. Liu Y, Luo Y, Chu G W, Luo J Z, Arowo M, Chen J F. 3D numerical simulation of a rotating packed bed with structured stainless steel wire mesh packing. *Chemical Engineering Science*, 2017, 170: 365–377
28. Jeon S S, Kim S J, Park G C. Numerical study of condensing bubble in subcooled boiling flow using volume of fluid model. *Chemical Engineering Science*, 2011, 66(23): 5899–5909
29. Yang Y C, Xiang Y, Chu G W, Zou H K, Sun B C, Arowo M, Chen J F. CFD modeling of gas–liquid mass transfer process in a rotating packed bed. *Chemical Engineering Journal*, 2016, 294: 111–121
30. Su M J, Luo Y, Chu G W, Cai Y, Le Y, Zhang L L, Chen J F. Dispersion behaviors of droplet impacting on wire mesh and process intensification by surface micro/nano-structure. *Chemical Engineering Science*, 2020, 219: 115593
31. Shih T H, Liou W W, Shabbir A, Yang Z G, Zhu J. A new  $k-\epsilon$  eddy viscosity model for high Reynolds number turbulent flows. *Computers & Fluids*, 1995, 24(3): 227–238